

Spectral analysis of multidimensional current-driven plasma instabilities and turbulence in hollow cathode plumes

By W. H. R. Chan[†], K. Hara, J. M. Wang, S. S. Jain, S. Mirjalili AND I. D. Boyd[†]

Large-amplitude current-driven instabilities in hollow cathode plumes can generate energetic ions responsible for cathode sputtering and spacecraft degradation. A 2D2V (two dimensions each in configuration [D] and velocity [V] spaces) grid-based Vlasov–Poisson (direct kinetic) solver is used to study their growth and saturation, which comprises four stages: linear growth, quasilinear resonance, nonlinear fill-in, and saturated turbulence. The linear modal growth rate, nonlinear saturation process, and ion velocity and energy distribution features in the turbulent regime are analyzed. Backstreaming ions are generated for large electron drifts, several ion acoustic periods after the potential field becomes turbulent. Interscale phase-space transfer and locality are analyzed for the Vlasov equation. The multidimensional study sheds light on the interactions between longitudinal and transverse plasma instabilities, as well as the inception of plasma turbulence.

1. Introduction

Hollow cathodes are crucial for the production of plasmas, and particularly electrons, in electric spacecraft thrusters. The erosion of cathode structures can limit the lifetime of outerspace missions by an order of magnitude to less than $O(10,000)$ hours (e.g., Friedly & Wilbur 1992; Kameyama & Wilbur 2000; Williams, Jr. *et al.* 2000; Mikellides *et al.* 2005, 2007, 2008; Goebel *et al.* 2007; Jorns *et al.* 2014; Lev *et al.* 2019). A key cause of such sputtering is the generation of fast ions at the cathode orifice, with energies corresponding to up to 100 eV (Friedly & Wilbur 1992; Williams & Wilbur 1992; Kameyama & Wilbur 2000; Williams, Jr. *et al.* 2000; Boyd & Crofton 2004; Goebel *et al.* 2007; Mikellides *et al.* 2008; Farnell *et al.* 2011). These high-energy ions are currently postulated to arise in part from collisionless and electrostatic current-carrying instabilities (Williams, Jr. *et al.* 2000; Mikellides *et al.* 2005, 2007, 2008; Goebel *et al.* 2007; Jorns *et al.* 2014; Lopez Ortega & Mikellides 2016; Jorns *et al.* 2017; Sary *et al.* 2017a,b; Hara & Hanquist 2018; Lopez Ortega *et al.* 2018; Hara 2019). The generation of axially energetic ions has been numerically investigated through grid-based Vlasov–Poisson (direct kinetic) simulations in a single spatial dimension (1D) (Hara & Treece 2019; Vazsonyi *et al.* 2020). We extend the analysis to two spatial dimensions (2D) to probe transversely (radially) energetic ions, whose presence has been observed experimentally (Boyd & Crofton 2004; Goebel *et al.* 2007; Farnell *et al.* 2011; Hall *et al.* 2019). Such ions are already deflected from the centerline from their inception and can impinge spacecraft more easily.

Two categories of current-carrying instabilities in fully ionized plasmas are typically considered (Omura *et al.* 2003; Mikellides *et al.* 2005). The ion acoustic instability manifests when the electron drift speed U_e exceeds the Bohm speed $\sqrt{k_B T_e / m_i}$ and $T_e \gg T_i$,

[†] Department of Aerospace Engineering Sciences, University of Colorado Boulder

where k_B , T_e , T_i , and m_i are the Boltzmann constant, electron temperature, ion temperature, and ion mass, respectively (Stringer 1964 and references therein). Physically, ion oscillations are excited by the net electron drift. Over a broad range of T_i/T_e , the Buneman instability arises when $U_e \gtrsim c_e = \sqrt{k_B T_e/m_e}$, where c_e and m_e are the electron thermal speed and electron mass, respectively (Buneman 1959). For 1D, the threshold is about $U_e \geq 1.3c_e$. Physically, electron oscillations are excited by the net electron drift. We consider $T_e/T_i = 10$, which is representative of cathode operating conditions (Goebel *et al.* 2005; Mikellides *et al.* 2005, 2007, 2008; Farnell *et al.* 2011; Jorns *et al.* 2017). Here, both instabilities can be physically relevant depending on U_e . We build on previous studies of the two-dimensional Buneman instability (Amano & Hoshino 2009) but focus on ion acceleration instead of electron acceleration and use a physical mass ratio corresponding to a hydrogen plasma ($m_i/m_e = 1.8229 \times 10^3$).

The objective of this work is to analyze the stages of instability growth, as well as the inception of multidimensional plasma turbulence and its spectral characteristics. In Section 2, we describe our computational and physical setup. In Section 3, we revisit key results from the simpler 1D instability to obtain physical insights. These are used to interpret results of the 2D instability in Section 4. Conclusions are provided in Section 5.

2. Methodology

2.1. Direct kinetic solver

The direct kinetic solver employed here was originally developed at the University of Michigan with verification and validation against canonical and complex plasma problems, such as waves, electron-emitting sheaths, and Hall thruster discharges (Hara & Hanquist 2018; Raisanen *et al.* 2019; Vazsonyi *et al.* 2020; and references therein). In contrast to state-of-the-art particle-in-cell solvers, direct kinetic solvers eliminate statistical noise and are suitable for investigating instability growth and turbulence inception. Under the electrostatic approximation, the solver computes the time evolution of the probability density function, f_* , for some particle type $* = i, e$ (ions, electrons) according to the following transport equation

$$\frac{\partial f_*(\mathbf{x}, \mathbf{v}; t)}{\partial t} + \mathbf{v} \cdot \nabla_{\mathbf{x}} f_*(\mathbf{x}, \mathbf{v}; t) + \frac{q_* \mathbf{E}}{m_*} \cdot \nabla_{\mathbf{v}} f_*(\mathbf{x}, \mathbf{v}; t) = 0, \quad (2.1)$$

where \mathbf{x} , \mathbf{v} , and \mathbf{E} respectively denote the position, velocity, and electric field vectors, q_* denotes the charge of the simulated particle type, and t denotes the time. The computational domain is discretized in \mathbf{x} - \mathbf{v} space with a parallelized second-order finite-volume method, which is described by Chan & Boyd (2022a,b). Gauss's law is expressed using $\mathbf{E} = -\nabla_{\mathbf{x}} \phi$ as a Poisson equation for the electric potential ϕ of the form

$$\nabla_{\mathbf{x}}^2 \phi = -\frac{e(n_i - n_e)}{\varepsilon_0}, \quad (2.2)$$

where ε_0 and e respectively denote the vacuum permittivity and elementary charge, and n_i and n_e respectively denote the ion and electron number densities

$$n_i(\mathbf{x}; t) = \int_{\mathbf{v}} f_i(\mathbf{x}, \mathbf{v}'; t) d\mathbf{v}'; \quad n_e(\mathbf{x}; t) = \int_{\mathbf{v}} f_e(\mathbf{x}, \mathbf{v}'; t) d\mathbf{v}'. \quad (2.3)$$

Periodic and no-flux boundary conditions are employed for \mathbf{x} and \mathbf{v} , respectively.

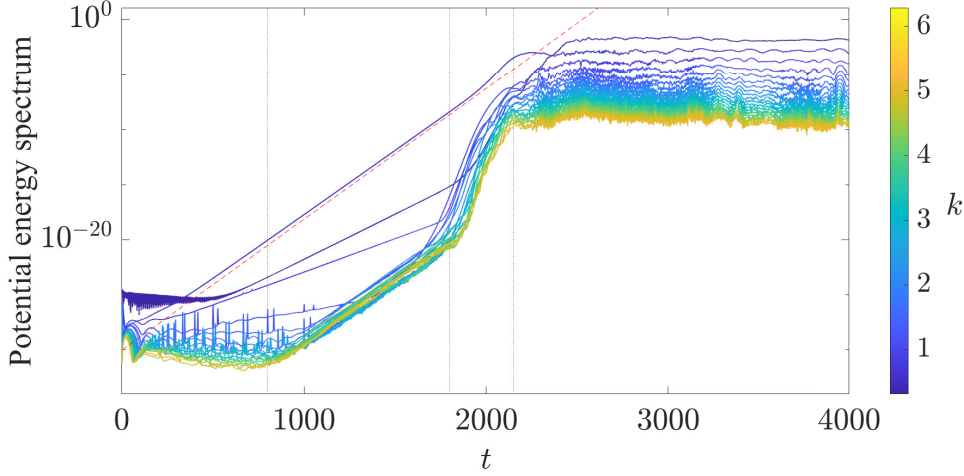


FIGURE 1. Time evolution of the ensemble-averaged electrostatic potential energy spectrum. Field strengths are normalized by $\phi_{\text{th}}/\lambda_{\text{D}}$, where $\phi_{\text{th}} = k_{\text{B}}T_e/e$ is the thermal potential. Hereinafter, lengths and times are nondimensionalized by λ_{D} and $1/\omega_e$, respectively. The sloped dashed line denotes the maximum growth rate obtained from Eq. (2.4), while the vertical dotted lines qualitatively demarcate different evolution stages. Every fifth mode is plotted and the curves are colored from blue to yellow (dark to light in grayscale) in increasing k .

2.2. Problem setup and linear stability analysis

We consider 1D1V and 2D2V current-carrying instabilities, where D and V denote the configuration and velocity spaces, respectively. The corresponding simulations are respectively two- and four-dimensional. Since these are long-wavelength instabilities, we choose domain lengths sufficiently larger than the Debye length, $\lambda_{\text{D}} = \sqrt{(\varepsilon_0 k_{\text{B}} T_e)/(n_e e^2)}$. The species temperatures are $T_i = 0.2$ eV and $T_e = 2$ eV, the electrons have a net axial drift described by the initial electron Mach number $M_{e,d} = U_e/c_{e,d}$, and the ions have zero initial mean speed. Lengths and velocities are respectively nondimensionalized by λ_{D} and the s -dimensional thermal speed, $c_{*,s} = \sqrt{s k_{\text{B}} T_*/m_*}$ (so $M_e = M_{e,1}$ and $c_* = c_{*,1}$), while time is nondimensionalized by the inverse electron frequency $1/\omega_e = \lambda_{\text{D}}/c_e$.

Linear growth rates for the current-carrying instability can be analytically predicted via solution of the (dimensional) linear dispersion relation for electrostatic waves

$$1 + \sum_* \frac{\omega_*^2}{c_*^2 k^2} \left[1 + \left(\frac{\omega}{\sqrt{2} c_* k} - \frac{\delta_{*e} M_{e,1} \cos \theta}{\sqrt{2}} \right) Z \left(\frac{\omega}{\sqrt{2} c_* k} - \frac{\delta_{*e} M_{e,1} \cos \theta}{\sqrt{2}} \right) \right] = 0, \quad (2.4)$$

where $k = |\mathbf{k}|$ and ω are, respectively, the modal wavenumber magnitude and angular frequency, θ is the angle between \mathbf{k} and the axial direction x , $\omega_* = \sqrt{(n_* e^2)/(m_* \varepsilon_0)}$ is the plasma frequency, $c_* = \sqrt{k_{\text{B}} T_*/m_*}$, and Z is the plasma dispersion function

$$Z(\xi) = \frac{1}{\sqrt{\pi}} \int_{-\infty}^{\infty} \frac{e^{-z^2}}{z - \xi} dz = i\sqrt{\pi} e^{-\xi^2} \operatorname{erfc}(-i\xi); \quad \frac{dZ(\xi)}{d\xi} = -2[1 + \xi Z(\xi)]. \quad (2.5)$$

3. 1D current-carrying instability

To interpret the 2D current-carrying instability more easily, we first discuss pertinent results of the 1D instability. Six 1D1V simulations with domain extents $x \in [0, 100]$, $v_{x,i} \in [-32, 32]$, $v_{x,e} \in [-6, 6]$ and resolutions $\Delta x = 1/10$, $\Delta v_{x,i} = 1/25$, $\Delta v_{x,e} = 1/100$ for the

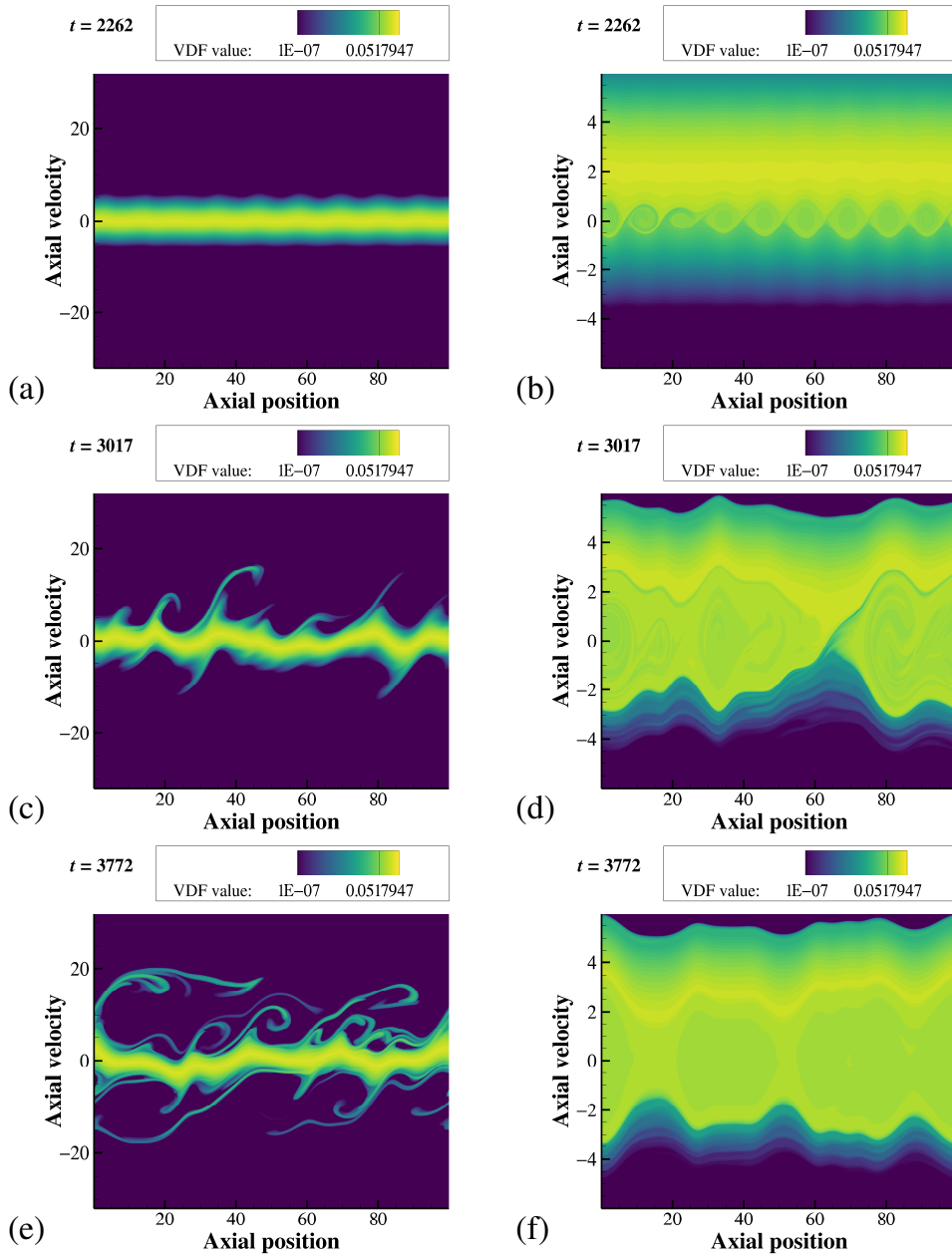


FIGURE 2. Ion (a,c,e) and electron (b,d,f) velocity distribution functions (VDFs), normalized by the initial spatially uniform number density, at $t = 2.3 \times 10^3$ (a,b), 3.0×10^3 (c,d), and 3.8×10^3 (e,f). Note that the contours are logarithmically spaced.

spatial, ion velocity, and electron velocity dimensions, respectively, were performed with $\Delta t = 0.016$ and $M_{e,1} = 2.0$ in line with the grid-point recommendations of Chan & Boyd (2022a) for instability resolution. The time evolution of the ensemble-averaged electrostatic potential energy spectrum, obtained through a Fourier decomposition of ϕ , is plotted in Figure 1. Four stages of evolution are discernible. Modes first grow

linearly at their analytically predicted modal growth rates. Harmonics then interact with the fastest-growing fundamental to grow at a comparable rate. The remaining modes eventually experience accelerated growth, filling in the intermediate wavenumbers to form a saturated and persistent broadband spectrum. The growth of harmonics (locking) and subsequent fill-in are features of turbulence also seen in, e.g., hydrodynamic simulations of turbulent boundary layers. Note that larger modes always lead and exceed smaller modes, possibly casting in doubt the existence of an inverse energy cascade.

Figure 2 plots the ion and electron velocity distribution functions at three time instances: one in the third stage (nonlinear fill-in) and two in the fourth stage (saturated turbulence). Clockwise vortical motion represents trapping. The excitation of trapped electron oscillations precedes the generation of high-energy ions. Forward-streaming ions and electrons are sustained at the early stage of saturated turbulence, with backward-streaming ions and electrons following about $O(10)$ ion oscillation periods after.

3.1. Interscale phase-space transfer and locality

Preliminary analysis of interscale transfer of f_i is performed for 1D1V phase space through analysis of the following transport equation for the filtered ion variance $\overline{f_i^2}/2$

$$\begin{aligned} \frac{\partial}{\partial t} \left(\frac{1}{2} \overline{f_i^2} \right) + \frac{\partial}{\partial x} \left(\overline{v} \cdot \frac{1}{2} \overline{f_i^2} \right) + \frac{q_i}{m_i} \frac{\partial}{\partial v} \left(\overline{E} \cdot \frac{1}{2} \overline{f_i^2} \right) = - \frac{\partial}{\partial x} \left[\overline{f_i} (\overline{v f_i} - \overline{v} \overline{f_i}) \right] - \\ - \frac{q_i}{m_i} \frac{\partial}{\partial v} \left[\overline{f_i} (\overline{E f_i} - \overline{E} \overline{f_i}) \right] + (\overline{v f_i} - \overline{v} \overline{f_i}) \frac{\partial \overline{f_i}}{\partial x} + \frac{q_i}{m_i} (\overline{E f_i} - \overline{E} \overline{f_i}) \frac{\partial \overline{f_i}}{\partial v}. \end{aligned} \quad (3.1)$$

The last two terms are denoted $\overline{T_x}$ and $\overline{T_v}$, and represent interscale transfer due to transport in the physical and velocity spaces, respectively. The overbar denotes a filtering operation, which is performed here with the assistance of a discrete wavelet decomposition. The ion distribution function f_i may be written as (cf. Kim *et al.* 2018)

$$f_i(x, v) = \sum_{s=1}^{\mathcal{S}} \sum_{d=1}^3 \sum_{x_s, v_s} \check{f}^{(s,d)}(x_s, v_s) \mathcal{G}^{(s,d)}(x - x_s, v - v_s) + \sum_{x_{\mathcal{S}}, v_{\mathcal{S}}} \hat{f}^{(\mathcal{S})} \mathcal{H}^{(\mathcal{S})}(x - x_{\mathcal{S}}, v - v_{\mathcal{S}}), \quad (3.2)$$

where s and \mathcal{S} respectively denote the scale index and number of scales, d is a wavelet directionality index, $\mathcal{G}^{(s,d)}$ and $\mathcal{H}^{(s)}$ respectively denote the wavelet and scaling functions, and $\check{f}^{(s,d)}$ and $\hat{f}^{(s)}$ respectively denote the detail and approximation coefficients. Here, the Haar wavelet is used and the Vlasov simulation is performed with 1,024 points in each dimension so that $\mathcal{S} = 10$. Then, $\overline{f_i^{(\sigma)}}$ is defined for $\sigma = 1, \dots, \mathcal{S}$ as

$$\overline{f_i^{(\sigma)}}(x, v) = \sum_{s=\sigma}^{\mathcal{S}} \sum_{d=1}^3 \sum_{x_s, v_s} \check{f}^{(s,d)}(x_s, v_s) \mathcal{G}^{(s,d)}(x - x_s, v - v_s) + \sum_{x_{\mathcal{S}}, v_{\mathcal{S}}} \hat{f}^{(\mathcal{S})} \mathcal{H}^{(\mathcal{S})}(x - x_{\mathcal{S}}, v - v_{\mathcal{S}}). \quad (3.3)$$

Figure 3 plots $\overline{T_v^{(\sigma)}} - \overline{T_v^{(\sigma+1)}}(v)$, averaged over all x , late $t \in [3.8 \times 10^3, 7.6 \times 10^3]$, and 40 ensemble realizations. This represents the ion variance gained or lost at velocity v and scale σ due to transfer between velocities and scales. The corresponding spatial interscale term is negligible in comparison (not shown here). At these late times, interscale transfer is biased towards negative velocities, as backward-streaming ions are formed on average after forward-streaming ions. The limited correlation between large and small scales hints at interscale locality, which may be verified through an information-theoretic approach analyzing causality (Lozano-Durán & Arranz 2022).

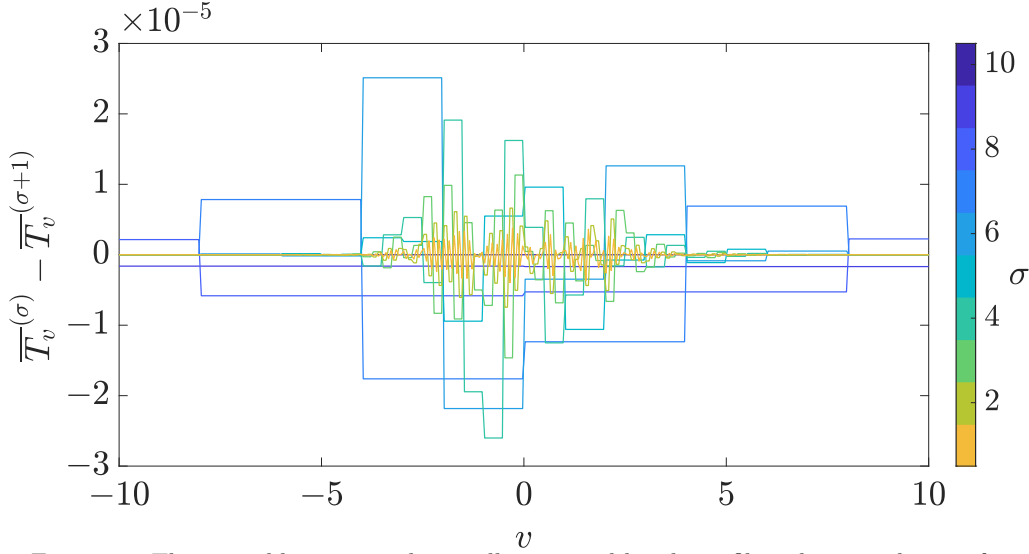


FIGURE 3. The ensemble, time, and spatially averaged bandpass-filtered interscale transfer term due to velocity transport at different scales σ .

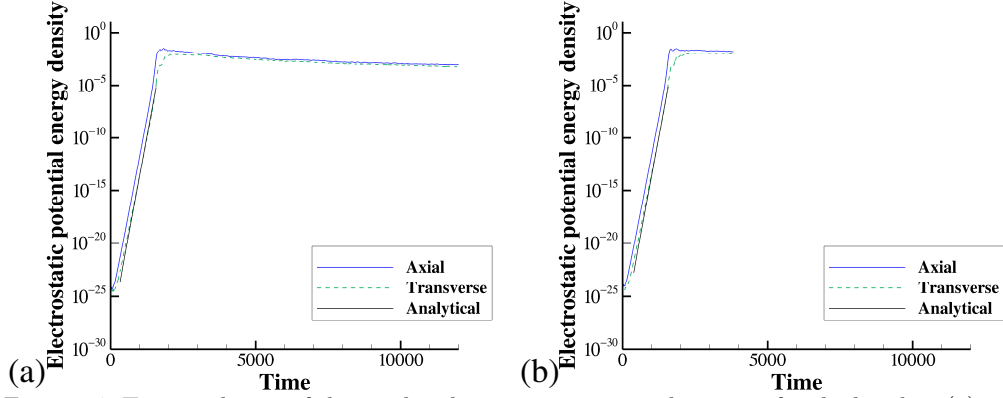


FIGURE 4. Time evolution of the axial and transverse potential energies for the baseline (a) and velocity-refined (b) simulations. The analytical line denotes the growth rate from Eq. (2.4).

4. 2D current-carrying instability

Building on the preliminary work of Vazsonyi (2021), the 2D2V instability is simulated with domain extents $x, y \in [0, 80]$, $v_{x,i}, v_{y,i} \in [-32, 32]$, $v_{x,e}, v_{y,e} \in [-6, 6]$ and resolutions $\Delta x = \Delta y = 1/2.5$, $\Delta v_{x,i} = \Delta v_{y,i} = 1/2$, $\Delta v_{x,e} = \Delta v_{y,e} = 1/16$ for the spatial, ion velocity, and electron velocity dimensions, respectively. A second simulation was performed with twice the resolution in all velocity dimensions to ascertain velocity grid convergence, given that resolutions are decreased from the 1D case for computational tractability. The simulation is converged with respect to the spatial grid and domain extent for the quantities of interest (not shown here). Both simulations were performed with $\Delta t = 0.062$ and $M_{e,2} = 1.6$ (so $M_{e,1} = 2.3$). Figure 4 plots the time evolution of the axial and transverse potential energies, respectively, $\sum E_x^2/2$ and $\sum E_y^2/2$, where E_x and E_y are the axial and transverse electric field strengths in each cell. The baseline resolution is seen to exhibit grid convergence and is analyzed for the remainder of this work.

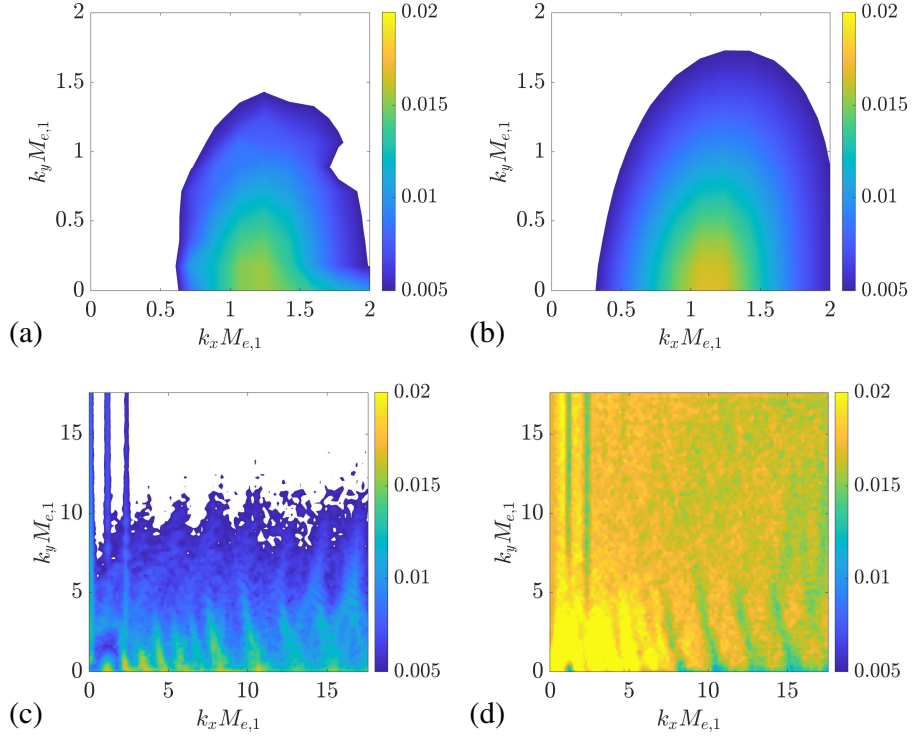


FIGURE 5. Numerical growth rates of spectral modes $\{k_x M_{e,1}, k_y M_{e,1}\}$ of the electric potential spectrum $E_{\phi\phi}$ for $t = [0, 3.8 \times 10^2]$ (a), $[3.8 \times 10^2, 1.1 \times 10^3]$ (c), and $[1.1 \times 10^3, 1.9 \times 10^3]$ (d), obtained via linear regression. The maximum growth rate predicted by Eq. (2.4) is 0.017, and the corresponding analytical modal growth rates are plotted in (b). Growth rates less than 5×10^{-3} are excluded to remove cases where oscillations confound the regression.

Figure 5 plots the modal growth rates in time intervals qualitatively corresponding to the four stages identified in Figure 1. The wavenumbers are multiplied by $M_{e,1}$ for direct comparison with Amano & Hoshino (2009), particularly the linear stage in Figure 5(a,b). The same qualitative trends are observed in 1D and 2D: linear growth as described by Eq. (2.4), subsequent comparable growth of harmonics, nonlinear fill-in of intermediate wavenumbers via a catch-up mechanism, and eventually saturated turbulence.

Figure 6 plots several representative ion and electron velocity and energy distribution functions. Electron trapping and isotropization occur more rapidly than their corresponding ion processes owing to the larger thermal speed and smaller response time of electrons. High-energy ions are generated in abundance at equivalent temperatures of between 20 and 50 eV with practical relevance to hollow cathode sputtering.

5. Conclusions

The investigation of current-driven plasma instabilities is crucial to determine the origin and fluxes of high-energy ions that cause hollow cathode erosion in electric spacecraft thrusters. A direct kinetic solver is used to study the evolution of the ion and electron velocity distribution functions without contamination from statistical noise inherent in

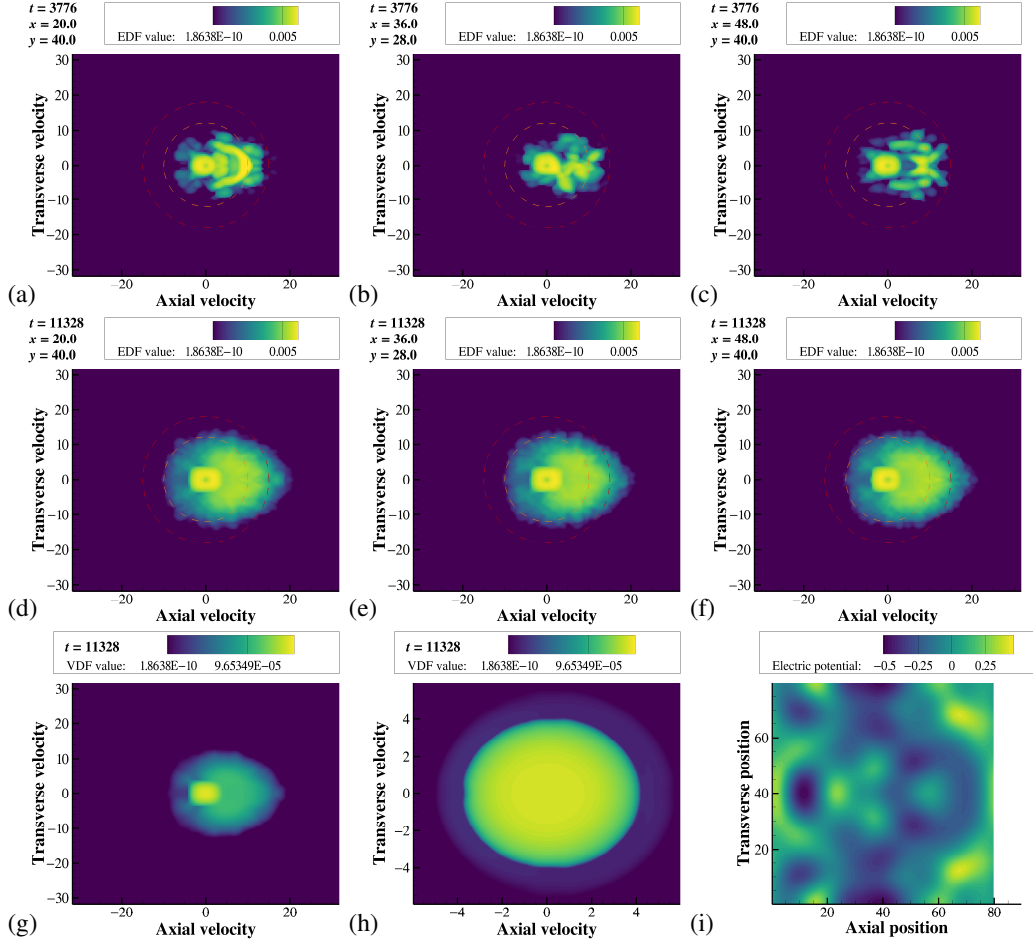


FIGURE 6. Local ion energy distribution functions (EDFs) at three different locations at $t = 3.8 \times 10^3$ (a,b,c) and $t = 1.1 \times 10^4$ (d,e,f). The spatially averaged ion (g) and electron (h) velocity distribution functions (VDFs), as well as the electric potential profile (i), are also plotted for $t = 1.1 \times 10^4$. The contours in (a–h) are logarithmically spaced, and the two concentric circles in (a–f) represent 20 and 45 eV contours.

state-of-the-art particle methods. Both 1D and 2D current-driven instabilities exhibit four developmental stages: linear growth, quasilinear resonance, nonlinear fill-in, and saturated turbulence. The maximum linear modal growth rate matches analytical predictions from the linear plasma dispersion relation. Harmonics of the fastest-growing fundamental, followed by intermediate wavenumbers, grow in a process that resembles the development of hydrodynamic turbulence. 2D instabilities further exhibit a return to isotropy also reminiscent of classical fluid behavior. However, unlike hydrodynamic turbulence, which only fully emerges in 3D, such plasma turbulence occurs even in 1D and 2D instabilities as postulated by Buneman (1959) since ions and electrons are allowed to interpenetrate unlike fluids. While the potential energy quickly saturates in the turbulent regime, backward-streaming ions are only formed after several ion trapping cycles. More generally, direct kinetic solvers can be used to provide quantitative predictions of cathode sputtering rates and potential fluctuations observable in experiments.

Acknowledgments

The authors would like to acknowledge K. Griffin, K. Schneider, K. Matsuda, and the multiphase group at the CTR Summer Program for helpful discussions. This work utilized the Blanca condo computing resource of the University of Colorado, as well as the Summit supercomputer, which is supported by the National Science Foundation (awards ACI-1532235 and ACI-1532236), the University of Colorado, and Colorado State University.

REFERENCES

- AMANO, T. & HOSHINO, M. 2009 Nonlinear evolution of Buneman instability and its implication for electron acceleration in high Mach number collisionless perpendicular shocks. *Phys. Plasmas* **16**, 102901.
- BOYD, I. D. & CROFTON, M. W. 2004 Modeling the plasma plume of a hollow cathode. *J. Appl. Phys.* **95**, 3285–3296.
- BUNEMAN, O. 1959 Dissipation of currents in ionized media. *Phys. Rev.* **115**, 503–517.
- CHAN, W. H. R. & BOYD, I. D. 2022a Grid-point requirements for direct kinetic simulation of weakly collisional plasma plume expansion. *J. Comput. Phys.*, under review.
- CHAN, W. H. R. & BOYD, I. D. 2022b Enabling direct kinetic simulation of dense plasma plume expansion for laser ablation plasma thrusters. *J. Electr. Propul.* **1**, 26.
- FARNELL, C. C., WILLIAMS, J. D. & FARNELL, C. C. 2011 Comparison of hollow cathode discharge plasma configurations. *Plasma Sources Sci. T.* **20**, 025006.
- FRIEDLY, V. J. & WILBUR, P. J. 1992 High current hollow cathode phenomena. *J. Propul. Power* **8**, 635–643.
- GOEBEL, D. M., JAMESON, K. K., WATKINS, R. M., KATZ, I. & MIKELLIDES, I. G. 2005 Hollow cathode theory and experiment. I. Plasma characterization using fast miniature scanning probes. *J. Appl. Phys.* **98**, 113302.
- GOEBEL, D. M., JAMESON, K. K., KATZ, I. & MIKELLIDES, I. G. 2007 Potential fluctuations and energetic ion production in hollow cathode discharges. *Phys. Plasmas* **14**, 103508.
- HALL, S. J., GRAY, T. G., YIM, J. T., CHOI, M., MOONEY, M. M., SARVER-VERHEY, T. R. & KAMHAWI, H. 2019 The effect of a Hall thruster-like magnetic field on operation of a 25-A class hollow cathode. *36th International Electric Propulsion Conference*, IEPC-2019-300.
- HARA, K. 2019 An overview of discharge plasma modeling for Hall effect thrusters. *Plasma Sources Sci. T.* **28**, 044001.
- HARA, K. & HANQUIST, K. 2018 Test cases for grid-based direct kinetic modeling of plasma flows. *Plasma Sources Sci. T.* **27**, 065004.
- HARA, K. & TREECE, C. 2019 Ion kinetics and nonlinear saturation of current-driven instabilities relevant to hollow cathode plasmas. *Plasma Sources Sci. T.* **28**, 055013.
- JORNS, B. A., MIKELLIDES, I. G. & GOEBEL, D. M. 2014 Ion acoustic turbulence in a 100-A LaB₆ hollow cathode. *Phys. Rev. E* **90**, 063106.
- JORNS, B. A., DODSON, C., GOEBEL, D. M. & WIRZ, R. 2017 Propagation of ion acoustic wave energy in the plume of a high-current LaB₆ hollow cathode. *Phys. Rev. E* **96**, 023208.
- KAMEYAMA, I. & WILBUR, P. J. 2000 Measurements of ions from high-current hollow cathodes using electrostatic energy analyzer. *J. Propul. Power* **16**, 529–535.

- KIM, J., BASSENNE, M., TOWERY, C. A. Z., HAMLINGTON, P. E., POLUDNENKO, A. Y. & URZAY, J. 2018 Spatially localized multi-scale energy transfer in turbulent premixed combustion. *J. Fluid Mech.* **848**, 78–116.
- LEV, D. R., MIKELLIDES, I. G., PEDRINI, D., GOEBEL, D. M., JORNS, B. A. & McDONALD, M. S. 2019 Recent progress in research and development of hollow cathodes for electric propulsion. *Rev. Mod. Plasma Phys.* **3**, 6.
- LOPEZ ORTEGA, A. & MIKELLIDES, I. G. 2016 The importance of the cathode plume and its interactions with the ion beam in numerical simulations of Hall thrusters. *Phys. Plasmas* **23**, 043515.
- LOPEZ ORTEGA, A., JORNS, B. A. & MIKELLIDES, I. G. 2018 Hollow cathode simulations with a first-principles model of ion-acoustic anomalous resistivity. *J. Propul. Power* **34**, 1026–1038.
- LOZANO-DURÁN, A. & ARRANZ, G. 2022 Information-theoretic formulation of dynamical systems: causality, modeling, and control. *Phys. Rev. Res.* **4**, 023195.
- MIKELLIDES, I. G., KATZ, I., GOEBEL, D. M. & POLK, J. E. 2005 Hollow cathode theory and experiment. II. A two-dimensional theoretical model of the emitter region. *J. Appl. Phys.* **98**, 113303.
- MIKELLIDES, I. G., KATZ, I., GOEBEL, D. M. & JAMESON, K. K. 2007 Evidence of nonclassical plasma transport in hollow cathodes for electric propulsion. *J. Appl. Phys.* **101**, 063301.
- MIKELLIDES, I. G., KATZ, I., GOEBEL, D. M., JAMESON, K. K. & POLK, J. E. 2008 Wear mechanisms in electron sources for ion propulsion, 2: Discharge hollow cathode. *J. Propul. Power* **24**, 866–879.
- OMURA, Y., HEIKKILA, W. J., UMEDA, T., NINOMIYA, K. & MATSUMOTO, H. 2003 Particle simulation of plasma response to an applied electric field parallel to magnetic field lines. *J. Geophys. Res.-Space* **108**, 1197.
- RAISANEN, A. R., HARA, K. & BOYD, I. D. 2019 Two-dimensional hybrid-direct kinetic simulation of a Hall thruster discharge plasma. *Phys. Plasmas* **26**, 123515.
- SARY, G., GARRIGUES, L. & BOEUF, J.-P. 2017a Hollow cathode modeling: I. A coupled plasma thermal two-dimensional model. *Plasma Sources Sci. T.* **26**, 055007.
- SARY, G., GARRIGUES, L. & BOEUF, J.-P. 2017b Hollow cathode modeling: II. Physical analysis and parametric study. *Plasma Sources Sci. T.* **26**, 055008.
- STRINGER, T. E. 1964 Electrostatic instabilities in current-carrying and counterstreaming plasmas. *J. Nucl. Energy C* **6**, 267–279.
- VAZSONYI, A. R. 2021 Deterministic-kinetic computational analyses of expansion flows and current-carrying plasmas. Ph.D. dissertation, University of Michigan.
- VAZSONYI, A. R., HARA, K. & BOYD, I. D. 2020 Non-monotonic double layers and electron two-stream instabilities resulting from intermittent ion acoustic wave growth. *Phys. Plasmas* **27**, 112303.
- WILLIAMS, J. D. & WILBUR, P. J. 1992 Electron emission from a hollow cathode-based plasma contactor. *J. Spacecraft Rockets* **29**, 820–829.
- WILLIAMS, JR., G. J., SMITH, T. B., DOMONKOS, M. T., GALLIMORE, A. D. & DRAKE, R. P. 2000 Laser-induced fluorescence characterization of ions emitted from hollow cathodes. *IEEE T. Plasma Sci.* **28**, 1664–1675.